Vol. 153: 25-36, 1997 | MARINE ECOLOGY PROGRESS SERIES Mar Ecol Prog Ser | Published July 10

Modelling the mud surface temperature on intertidal flats to investigate the spatio-temporal dynamics of the benthic microalgal photosynthetic capacity

J.-M. Guarini[1,*], G. F. Blanchard[1], Ph. Gros[2], S. J. Harrison[3]

[1]CNRS-IFREMER, Centre de Recherche en Ecologie Marine et Aquaculture de L'Houmeau, B.P. 5, F-17137 L'Houmeau, France
[2]IFREMER Centre de Brest, B.P. 70, F-29280 Plouzané, France
[3]University of Stirling Department of Environmental Science, Stirling FK9 4LA, Scotland, UK

ABSTRACT: The mud surface temperature (MST) of an intertidal mudflat in Marennes-Oléron Bay (France) and the biomass-specific photosynthetic capacity (P^B_{max}) of benthic microalgae were modelled to investigate their spatio-temporal dynamics. Simulations were performed over 2 different periods during and after the microphytobenthos spring bloom (April and June, respectively) and under 2 different tidal conditions (spring and neap tides). The deterministic MST model is based on thermodynamic processes. Comparison at different periods between measured data series and simulations clearly establishes the reliability of the model, thus allowing extrapolations over time and space. The spatio-temporal dynamics of MST is primarily controlled by the immersion-emersion alternation combined with the solar cycle, with a strong influence of the phase difference in their respective oscillations: the highest MSTs are achieved in summer in the highest parts of the mudflat, when spring low tide occurs at midday. Three relevant time scales characterize the MST dynamics: long-term (seasonal cycle), medium-term (lunar cycle) and short-term (solar and tidal cycles). Within that framework, the response of P^B_{max} to changes in MST depends upon T_{opt}, the optimum temperature for photosynthesis (T_{opt} = 25°C all year round). In April, when the MST values are below T_{opt}, P^B_{max} varies exponentially with MST at short time scales. Conversely, in June, when the range of MST partially exceeds T_{opt}, P^B_{max} is inhibited on most of the mudflat surface area (up to 75%). This thermo-inhibition is highest in summer, when low tide occurs at midday.

KEY WORDS: Microphytobenthos · Photosynthetic capacity · Mud surface temperature modelling · Intertidal mudflat · Physical-biological coupled models

INTRODUCTION

Extensive intertidal mudflats, a prominent geomorphological feature of estuaries and semi-enclosed bays, are characterized by high levels of benthic microalgal biomass and production (Colijn & de Jonge 1984, de Jonge & Colijn 1994) which supply both the benthic (Levinton & Bianchi 1981, Plante-Cuny & Plante 1986) and planktonic food webs (Baillie & Welsh 1980, de Jonge & van Beusekom 1992). Basically, 2 specific processes control the production of benthic microalgae in the intertidal environment. First, during the emersion period motile benthic microalgae migrate upwards at the surface of the sediment, and photosynthesize (Pinckney & Zingmark 1991) under light-saturated conditions (i.e. at P^B_{max}, the biomass-specific photosynthetic capacity), without being photoinhibited (Blanchard & Cariou-Le Gall 1994). Second, in the very thin photic layer of the sediment, microalgae form a mat (Paterson 1989), whose P^B_{max} depends upon the mud surface temperature (MST) (Blanchard et al. 1996, Blanchard & Guarini 1996). In temperate areas, the MST itself is subject to large variations during emersion, resulting from a combination of the seasonal, tidal and nycthemeral cycles (Harrison 1985, Harrison & Phizacklea 1987, Piccolo et al. 1993).

Unlike the role of microalgal vertical migration, the effect of MST variations on the dynamics of micro-

*E-mail: jmguari@ifremer.fr

algal community primary production has never been investigated. It is therefore necessary to address this issue in order to achieve a better understanding of the benthic primary productivity system. In order to study the effect of MST on the spatio-temporal dynamics of microphytobenthic P^{B}_{max}, instantaneous temperature variations were computed at nodes of a regular grid (500 m × 500 m) covering the area studied (ca 10 km × 4 km). This is achieved by using a thermodynamic model of heat energy balance (HEB) at the mud-air interface during the emersion period on one hand, and at the mud-water interface during immersion on the other hand (Vugts & Zimmerman 1985, van Boxel 1986, Harrison & Phizacklea 1987). A similar approach has already been applied to the description of temperature dynamics at the soil-air interface in terrestrial systems (e.g. Stathers et al. 1988, Pikul 1991), and at the sediment-water interface for shallow and stagnant waters (van Boxel 1986, Piccolo et al. 1993).

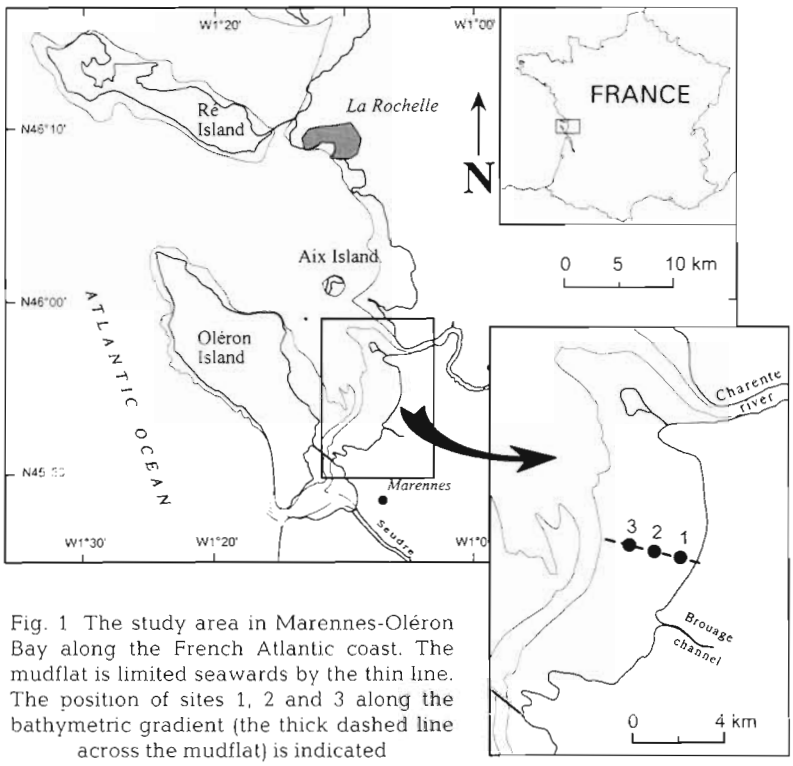

Fig. 1 The study area in Marennes-Oléron Bay along the French Atlantic coast. The mudflat is limited seawards by the thin line. The position of sites 1, 2 and 3 along the bathymetric gradient (the thick dashed line across the mudflat) is indicated

The objective of the present paper is thus 3-fold: (1) developing a model which describes MST spatio-temporal variations on a mudflat; (2) coupling the previous results with the mathematical relationship between the photosynthetic capacity of microphytobenthos and temperature (Blanchard et al. 1996), in order to provide spatialized time series of P^{B}_{max}; and then (3) analysing the spatio-temporal dynamics of microphytobenthic P^{B}_{max}. The study is primarily aimed at identifying the resulting effect of the tidal cycle, a strong oscillation forcing the dynamics of MST and P^{B}_{max}. In addition, 2 particular situations in the annual cycle of microphytobenthic biomass in Marennes-Oléron Bay are compared: the spring bloom in April, and the onset of the summer biomass decrease in June (Cariou-Le Gall & Blanchard 1995). As a matter of fact, the 2 cases are typical steps in the seasonal evolution of microphytobenthos on temperate intertidal mudflats.

MATERIAL AND METHODS

Study site. Marennes-Oléron Bay (Charente-Maritime, France) is located along the Atlantic coast (Fig. 1). The Bay is limited westwards by Oléron Island to the west and northwards by Aix Island and the mouth of the Charente estuary. This is the leading site in France for oyster production (50 000 t yr^{-1}), and the intertidal flats represent about 60 % of the total surface area of the Bay (170 km^2). The meteorological conditions exhibit a strong seasonality, typical of a temperate zone climate.

In addition, the tidal range reaches about 6 m during spring tides. Moreover, general hydrodynamic characteristics of the Bay of Biscay implies that low tide during spring tides always occurs at noon. As a consequence, the maximum emerged surface area of the mudflats coincides with the maximum supply of sunlight energy for a given period of time.

The mud temperature model. ***Vertical heat propagation equation within the sediment:*** At a given location of the intertidal mudflat, the temperature is assumed homogeneous in the horizontal dimensions. The general model of the mud temperature dynamics is thus restricted to a vertical heat propagation equation which can be assimilated to a diffusion process in a solid. Under the hypothesis of a vertical isotropy, the following parabolic equation (called the 'heat propagation equation') is then used (Priestley 1959, Harrison & Phizacklea 1987):

$$\rho_M C_{p_M} \frac{\partial T_M(z,t)}{\partial t} = \frac{\partial}{\partial z} \eta \frac{\partial T_M(z,t)}{\partial z} \qquad (1)$$

where ρ_M is the mass of mud per unit of volume (kg m^{-3}), C_{p_M} is the specific heat capacity of mud at constant pressure (J kg^{-1} K^{-1}), T_M is the temperature of the mud (K), z is depth (m), η is the conductivity (W m^{-1} K^{-1}), and t is time (s). The thermal diffusivity (m^2 s^{-1}) is $\mu = \eta / (\rho_M C_{p_M})$.

The value of μ lies in the range 10^{-7} to 10^{-5} m^2 s^{-1}; it depends on bioturbation whose effect is to increase ρ_M (Piccolo et al. 1993) which is the sum of the water fraction plus the dry sediment fraction [$\rho_M = \rho_W\xi + \rho_S(1-\xi)$, ξ being the mud porosity].

The boundary conditions at the surface are described by the heat energy balance (HEB) in alternating tidal conditions.

Boundary conditions at the surface: The temporal evolution of the mud temperature at the surface, $T_M(z_0,t)$, is governed by the first law of thermodynamics with the isobaric transformation:

$$\rho_M C_{P_M} \frac{\partial T_M(z_0,t)}{\partial t} = f\left(T_M(z_0,t)\right) \quad (2)$$

The right-hand term, $f\left(T_M(z_0,t)\right)$, is the HEB at the surface of the sediment. A value of 1 cm is assumed for the thickness of the surface layer where the temperature is homogeneous and governed by the HEB (Harrison & Phizacklea 1987, Piccolo et al. 1993).

(1) During the emersion period, HEB at the mud-air interface is the result of 5 heat exchange fluxes between mud and air, expressed in W m^{-2} (see Table 1 for processes, Table 2 for parameter values and Fig. 2 for the conceptual scheme): the fluxes of radiation coming from the sun (R_S), from the atmosphere (R_{Atm}, IR radiation), from the receiving surface (R_M), the sensible heat flux by conduction due to the difference between the temperature of mud and air ($S_{Mud\rightarrow Air}$), and the flux of evaporation (V_M) depending on the mud water content. So,

$$f\left(T_M(z_0,t)\right) = R_S + R_{Atm} - R_M - S_{Mud\rightarrow Air} - V_M$$

R_S and R_{Atm} are both energy inputs for the mud surface. R_S is forced in the model, while R_{Atm} is calculated using the Stephan-Boltzman function (see Table 1). Both fluxes are influenced by the nebulosity (attenuation due to cloud cover), which decreases R_S but increases R_{Atm} (Fig. 2); this antagonistic effect is accounted for by the attenuation coefficient k. The coefficient k is the ratio of R_S to the value R_{Sth} (Table 1), the latter being computed for a cloudless sky according to Brock (1981). During the whole night (i.e. $R_S = 0$), k is set at the average of the k values calculated for the 2 h period prior to darkness.

Calculation of R_M is also based on the Stephan-Boltzman function with an appropriate value of the emissivity coefficient of the mud (ε_M). Van Bavel & Hillel (1976) showed that ε_M is constant for water-saturated soil, which is always the case of intertidal mudflats (the water content of the surficial layer is higher than 50%).

$S_{Mud\rightarrow Air}$ is computed according to the bulk formula (Pond et al. 1974). The bulk formula gives more reliable results than the profile method (Businger 1973, Stathers et al. 1988), according to the comparison done by van Boxel (1986).

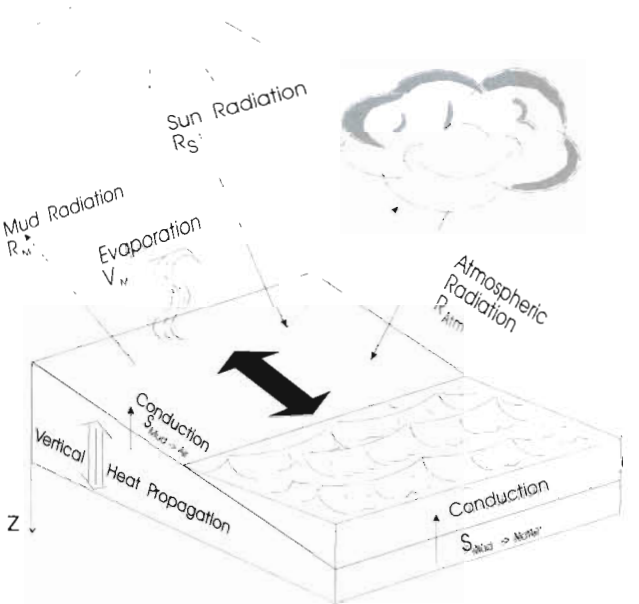

Fig. 2. Diagrammatic representation of heat exchange at the mud surface in the intertidal zone. The components of the heat energy balance (HEB) are symbolized by arrows, highlighting the differences in HEB between emersion and immersion periods. The heat propagation inside the sediment is also indicated

V_M is the product of the mud porosity (ξ; $\xi \in [0,1]$, dimensionless) and of the evaporative heat flux of a water mass, V_W:

$$V_M = \xi V_W$$

V_W is itself the product of the latent heat of evaporation L_V (the difference between enthalpies of water and air) and of the rate of evaporation (van Bavel & Hillel 1976). V_W is also given by a bulk formula depending on the ratio q_a/q_S (the measured relative humidity rate, see Table 1).

(2) During the immersion period, HEB at the mud-water interface is restricted to a sensible heat flux (Harrison 1985, Losordo & Piedrahita 1991) because the high turbidity of water hinders the penetration of light radiations (Fig. 2). The sensible heat flux is the product of the conductivity and of a finite-difference approximation of the temperature gradient between mud and overlying water (Losordo & Piedrahita 1991):

$$f\left(T_M(z_0,t)\right) = S_{Mud\rightarrow Water} = -\frac{\eta}{h_W}\left(T_M(z_0,t) - T_W(t)\right)$$

where η is the thermal conductivity (W m^{-1} K^{-1}) and h_W is the overlying water mixing height (m) with $h \approx 0.2H$ (H is the total height).

Table 1. Equations of the processes involved in the HEB at the mud-air interface and significance of the symbols used

Process	Symbol meaning
Atmospheric and solar radiation	
$R_{Sth} = R_0 \sin(h)(1 - A)$	R_0: solar constant
$R_{Atm} = \varepsilon_a \sigma T_a^4 (\zeta - k)$	h: sun height
$\varepsilon_A = 0.937 \times 10^{-5} T_a^2$	A: albedo
$k = \frac{R_S}{R_{Sth}}$	ε_a: emissivity of air
$\sin(h) = \sin(\delta)\sin(\phi) + \cos(\delta)\cos(\phi)\cos(AH)$	σ: Stephan-Boltzman constant
	T_a: measured air temperature
	ζ: constant ($2 \geq \zeta \geq 1$)
	k: attenuation coefficient
	δ: declination of the sun
	ϕ: latitude of the area
	AH: true horary angle
Mud radiation	
$R_M = \varepsilon_M \sigma T_M^4 (z_0, t)$	ε_M: emissivity of mud
Conduction	
$S_{Mud \to Air} = \rho_a C_{P_a} C_h (1 + U)(T_M(z_0, t) - T_a)$	ρ_a: mass of air per unit of volume
	C_{P_a}: specific heat of air at constant pressure
	C_h: bulk transfer coefficient for conduction
	U: wind speed measured at 10 m
Evaporation	
$V_W = \rho_a L_V C_V (1+U)\left[q_S\left(1 - \frac{q_a}{q_S}\right)\right]$	L_V: latent heat of evaporation
$L_V = [2500.84 - 2.35(T_E - 273.15)] \times 10^3$	C_V: bulk transfer coefficient for evaporation
$q_S = \frac{\lambda p_{sat}^V}{p_{Atm} - (1-\lambda) p_{sat}^V}$	q_S: specific humidity of saturated air at water temperature
	q_a: absolute air humidity
$p_{sat}^V = \exp\left\{2.3\left[\frac{7.5(T_E - 273.15)}{237.3 + (T_E - 273.15)} + 0.76\right]\right\}$	T_E: temperature of interstitial water (in equilibrium with mud temperature)
	λ: ratio between mass constant for dry air and mass constant for the vapor
	p_{sat}^V: vapor pressure in saturation at interstitial water temperature
	p_{Atm}: atmospheric pressure

Spatialization of the mud temperature model. The spatialization of the local equation (Eq. 1) with the boundary conditions (Eq. 2) is provided by an hydrodynamic model which calculates the total water height (H) by solving the continuous Saint-Venant 2DH equations (Le Hir et al. 1993). The numerical integration uses the ADI (Alternating Direction Implicit) method with a time step equal to 30 s and a spatial mesh (in horizontal dimensions) of 500 m × 500 m. Every 900 s (15 min) the local model of mud temperature is integrated at each node of the mesh grid. First, the boundary conditions differential equation (Eq. 2) at the mud surface is solved numerically using a fourth order Runge-Kutta algorithm. Secondly, the parabolic equation (Eq 1) is solved by a semi-implicit Cranck-Nicholson algorithm with a spatial step equal to 1 cm.

The boundary conditions $T_M(Z,t)$ at the depth Z = 100 cm are equal to the average daily water temperature. This represents the seasonal variations and the cumulative antecedence in the thermal baseline.

The values of the parameters used in the model are provided in Table 2.

Relationship between mud surface temperature and the photosynthetic capacity (P^B_{max}) of microphytobenthos. P^B_{max} (µg C (µg chl a)$^{-1}$ h^{-1}) is the maximum rate of inorganic carbon assimilation (per unit of biomass) under saturating light levels and in the absence of photoinhibition. P^B_{max} changes as a function of mud surface temperature [$T_M(z_0,t)$] according to the equation described in Blanchard et al. (1996):

$$P^B_{max}(T_M(z,t)) = P^B_{MAX}\left[\frac{T_{max} - T_M(z,t)}{T_{MAX} - T_{opt}}\right]^\beta \times \exp\left\{\beta\left(1 - \frac{T_{max} - T_M(z,t)}{T_{max} - T_{opt}}\right)\right\} \quad (3)$$

when $T_{opt} < T_{max}$ and $T_M(z,t) < T_{max}$

if $T_M(z,t) \geq T_{max}$, then $P^B_{max}(T_M(z,t)) = 0$.

P^B_{max} rises to a maximum value P^B_{MAX} [µg C (µg chl a)$^{-1}$ h^{-1}], reached at $T_M(z,t) = T_{opt}$, and beyond, decreases to zero [when $T_M(z,t) = T_{max}$]. β is a dimensionless parameter

The 4 parameters of Eq. (3) are identified by minimization of the ordinary least squares criterion (see

Table 2. Values and units of the model parameters (dash indicates a dimensionless parameter)

Parameter	Unit	Value
General equation		
η (conductivity)	W m^{-1} K^{-1}	0.80
ρ_S (soil volumetric mass)	kg m^{-3}	2650.0
ρ_W (water volumetric mass)	kg m^{-3}	1000.0
ξ (mud porosity)	–	0.55
Solar radiations		
R_0 (solar constant)	W m^{-2}	1353.00
A (Albedo)	–	0.08
Atmospheric radiation		
σ (Stephan-Boltzman)	W m^{-2} K^{-4}	5.67×10^{-8}
Mud radiation		
ε_M (mud emissivity)	–	0.96
Conduction		
ρ_a (air volumetric mass)	kg m^{-3}	1.2929
C_{P_a} (specific heat)	J kg^{-1} K^{-1}	1003.0
C_h (bulk coefficient)	–	0.0014
Evaporation		
C_V (bulk coefficient)	–	0.0014
λ (constant ratio)	–	0.621
Photosynthetic capacity		
T_{opt} (optimal temperature)	K	298.0
T_{max} (lethal temperature)	K	312.0
P^{B}_{MAX} (optimal P^{B}_{max})	μg C (μg chl *a*)$^{-1}$ h^{-1}	April: 11.2 June: 7.6
β	–	3.0

Blanchard et al. 1996). They were determined for each season (Blanchard et al. in press). T_{opt}, T_{max} and β are constant while P^{B}_{MAX} changes significantly (Table 2). The 2 situations of spring (April) and summer (June) are selected for the purpose of the present study.

Data measurements. Data series of both water and mud surface temperatures were recorded for the periods 19 to 27 March 1996, 15 to 24 May 1996 and 29 May to 8 June 1996 on a small mudflat area close to the laboratory. Instantaneous temperature values were sampled using 2 LI-COR 1000-15 temperature sensors connected to a LI-1000 DataLogger (precision ±0.5 K). Mud characteristics (porosity, grain size and mineralogy) are similar to those of the study area. The meteorological data series necessary to supply the mud temperature model were obtained from a neighbouring station.

RESULTS

Validation of the MST model

Unlike the other parameters (Table 2), the heat capacity of the mud (C_{P_M}) and the parameter ζ are not known in advance. They are estimated by minimization of the sum of squared differences between model output and time series of MST measurements (Fig. 3), using a simplex algorithm (Nelder & Mead 1965). Three different seasonal and meteorological conditions are used for the optimization: (1) the period 19 to 27 March, with an alternation of sunny and cloudy conditions; (2) the period 15 to 24 May, cloudy and cold; and (3) the period 29 May to 8 June, with warm temperatures and a cloudless sky.

For each MST time series, estimates of C_{P_M} and ζ as well as the mean square error (MSE) are reported in Table 3. The parameter estimates vary between periods (from 579.6 to 644.4 J kg^{-1} K^{-1} and from 1.53 to 1.86 for C_{P_M} and ζ, respectively) but the root MSE remains close to 1°C in every case, thus indicating good precision of the model. However, in order to handle only a single set of parameters applicable to the full range of meteorological situations, the 3 MST time series of Fig. 3 have been pooled together, and C_{P_M} and ζ have been estimated: 612 J kg^{-1} K^{-1} and 1.68, respectively (Table 3). It is worth noting that these estimates are very close to the average estimates calculated from the 3 independent periods (611.1 ± 23.0 J kg^{-1} K^{-1} and 1.68 ± 0.12, respectively). Furthermore, when estimates obtained from the pooled time series are applied to each MST time series independently, the mean quadratic error remains low: 1.05, 0.88 and 1.14°C for March, May and June, respectively. Therefore, under such a parameterization, the model predicts the MST evolution with a good precision for the range of weather conditions that are tested.

Fig. 3 presents a comparison between simulated and measured MST time series during the 3 different 10 d sampling periods at a single site on the mudflat. Overall, the model predicts with good accuracy the large and fast temperature fluctuations due to heating and cooling of the mud during the diurnal emersion and at the beginning of immersion, respectively. The maximum temperature daily change is 15°C at a rate of 2°C h^{-1} in March, 13°C at a rate of 2°C h^{-1} in May and 18°C at a rate of 3°C h^{-1} in June. Temperature maxima during emersion periods are 25, 26 and 34°C in March, May and June, respectively. The model tends to underestimate slightly the maxima (ca 1.5°C differences) in March (about half of the cases) and in May (only a few cases), but not in June; such discrepancies seem to be related to highly variable meteorological conditions.

During the night emersions, MST decreases are not well predicted by the model except in June when the sky is cloudless. This strongly suggests that the parameterization of the cloud cover effect by means of the coefficient *k* is not completely satisfactory. Nevertheless, this drawback has no effect on computation of

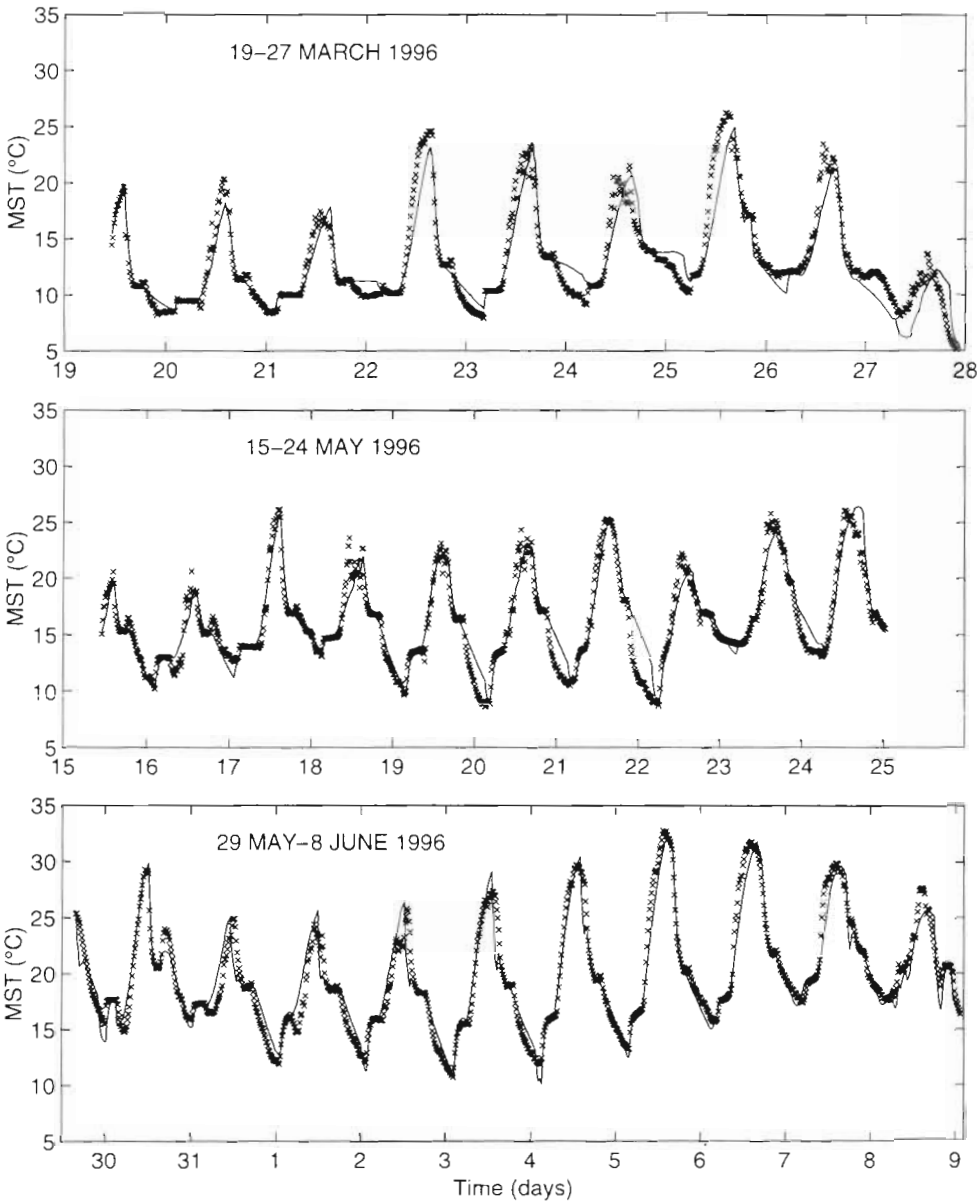

Fig. 3. Calibration of the MST model. The simulations (—) of MST are superimposed on the data series (×) measured at single points in 3 different periods: 19 to 27 March, 15 to 24 May and 29 May to 8 June

photosynthesis, since it only affects the accuracy of night MST predictions.

The June time series of MST is characterized by more constant meteorological conditions. The effect of the tidal cycle on mud temperature is thus clearly pointed out. From neap tide (31 May) when low tide occurs early in the morning, to spring tide (5 June) when low tide occurs at midday, the range of temperature change increases from 8°C (at a rate of 1°C h^{-1}) to 18°C (at a rate of 3°C h^{-1}) while temperature maximum raised from 25°C to 34°C. Then, from spring tide onwards, both the range and the maximum of MST decrease (Fig. 3) while low tide moves towards the afternoon. This pattern cannot be seen in March and May because the meteorological conditions are prevalent.

Spatio-temporal dynamics of MST and P^B_{max}

In order to point out the influence of the tidal oscillation on P^B_{max} dynamics, average meteorological conditions for each day of April and June 1996 were computed. This averaging cancels out the background noise due to high frequency fluctuations, especially within-day changes in cloudiness. Results of the simulation show 2 extreme situations for each month: the spring tide with low tide occurring at 12:00 h Universal Time (UT) (Figs. 4 & 6), and the neap tide with low tide occurring at 17:00 h UT (Figs. 5 & 7). In each case, the short-term variations of both MST and P^B_{max} are shown at 4 different times during the emersion period: Low tide −4, −2, +0 and +2 h, respectively.

Table 3. Estimates of C_{P_M} (J kg^{-1} K^{-1}) and ζ (dimensionless), and the corresponding mean squared error

Series	C_{P_M}	ζ	Root MSE
19–29 March	608.4	1.86	0.98
15–25 May	644.4	1.53	0.83
29 May–9 June	579.6	1.63	1.08
Pooled series	612.0	1.68	–

In April at spring tide, the MST difference between the highest and lowest levels of the emerged parts of the flat increases during ebb tide as the emerged surface area increases and as the mud is exposed for longer time (from 2°C at low tide –4 h to 14°C at low tide +2 h; Fig. 4). The temperature gradient is roughly uniform during ebb tide. At low tide the gradient is clearly not uniform: MST tends to homogeneize on high and mid-levels of the mudflat (where the highest MSTs are reached) and the gradient becomes steeper at the water front. During flood tide, the gradient becomes roughly uniform again: MST gets colder in the mid-level part of the flat and the flooding tide cools the surface mud (with a short equilibrium period) in the lowest part of the mudflat. The photosynthetic capacity of microphytobenthos exhibits very similar dynamics. The highest P^B_{max} [11.50 µg C (µg chl *a*)$^{-1}$ h^{-1}] and the largest gradient [7 µg C (µg chl *a*)$^{-1}$ h^{-1}] occur at low tide (Fig. 4). The maximum MST is reached (25°C at the highest level of the flat 2 h after low tide; Fig. 4) but does not exceed the optimal temperature for photosynthesis (Table 2).

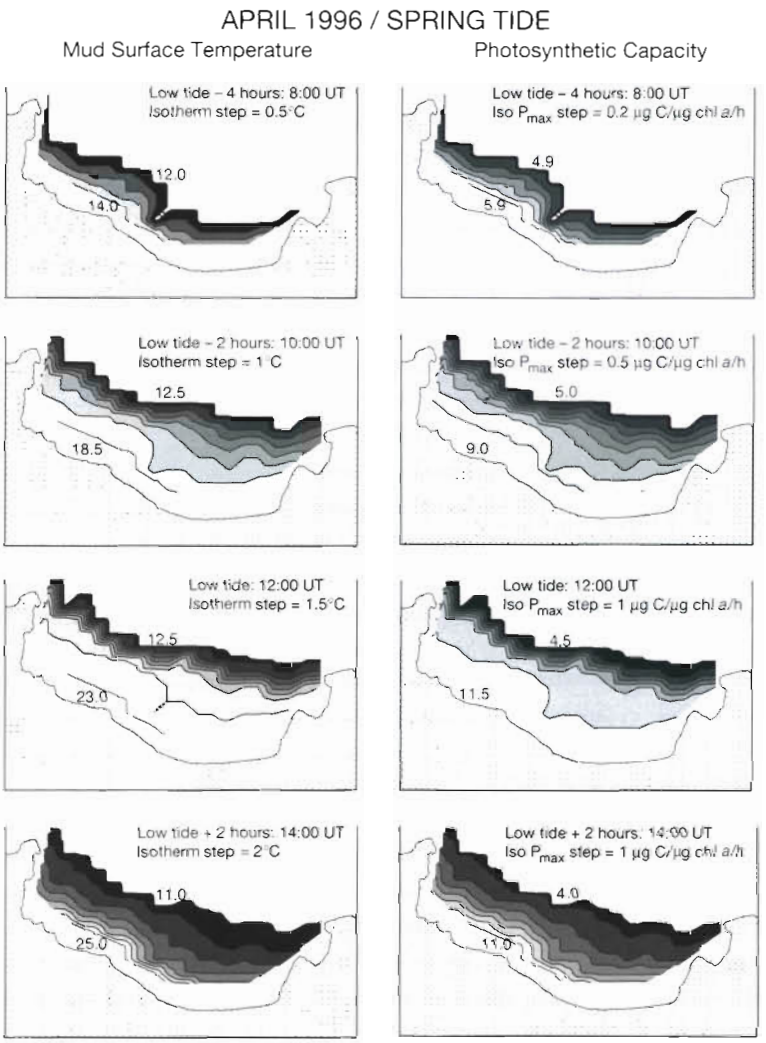

Fig. 4. Simulation of the spatio-temporal dynamics of MST (left-hand side) and P^B_{max} (right-hand side) in April 1996 at spring tide. Spatial distribution of computed values are shown at 4 different times during a diurnal emersion period: at low tide – 4 h, at low tide – 2 h, at low tide and at low tide + 2 h. The isotherm and iso-P^B_{max} steps are also provided

At neap tide, there are several differences with the spring tide pattern: (1) the maximal MST and P^B_{max} reach only 19°C and 8.50 µg C (µg chl *a*)$^{-1}$ h^{-1}, respectively, in the highest part of the emerged flat at 15:00 h UT during ebb tide; (2) MST starts to decrease before low tide; and (3) the MST gradient is not uniform and becomes steeper landwards instead of seawards. Otherwise, P^B_{max} and MST dynamics are also similar

In June, the dynamics of MST for both spring (Fig. 6) and neap tides (Fig. 7) is similar to the patterns described for April. The only difference concerns the maximum temperatures which are higher in June: 35°C at low tide +2 h during spring tide and 27.5°C at low tide –2 h during neap tide.

On the contrary, the dynamics of P^B_{max} is completely different. At spring tide, the maximum value of P^B_{max} is reached 2 h before low tide, and photosynthetic capacity values are similar over most of the emerged flat (Fig. 6). The spatial pattern is reversed, owing to a strong temperature inhibition of P^B_{max} (MST exceeds T_{opt}). The higher the topographic level, the stronger the thermo-inhibition. The maximum photosynthetic capacity [7.60 µg C (µg chl *a*)$^{-1}$ h^{-1}] moves downslope closer to the water front. Two hours after low tide, the inhibition is even more extensive [2.50 µg C (µg chl *a*)$^{-1}$ h^{-1}] in the highest fringe of the flat; otherwise, P^B_{max} tends to homogenize on the major part of the flat. At neap tide, a less extensive temperature inhibition appears 2 h before low tide only in the upper part of the flat, and persists

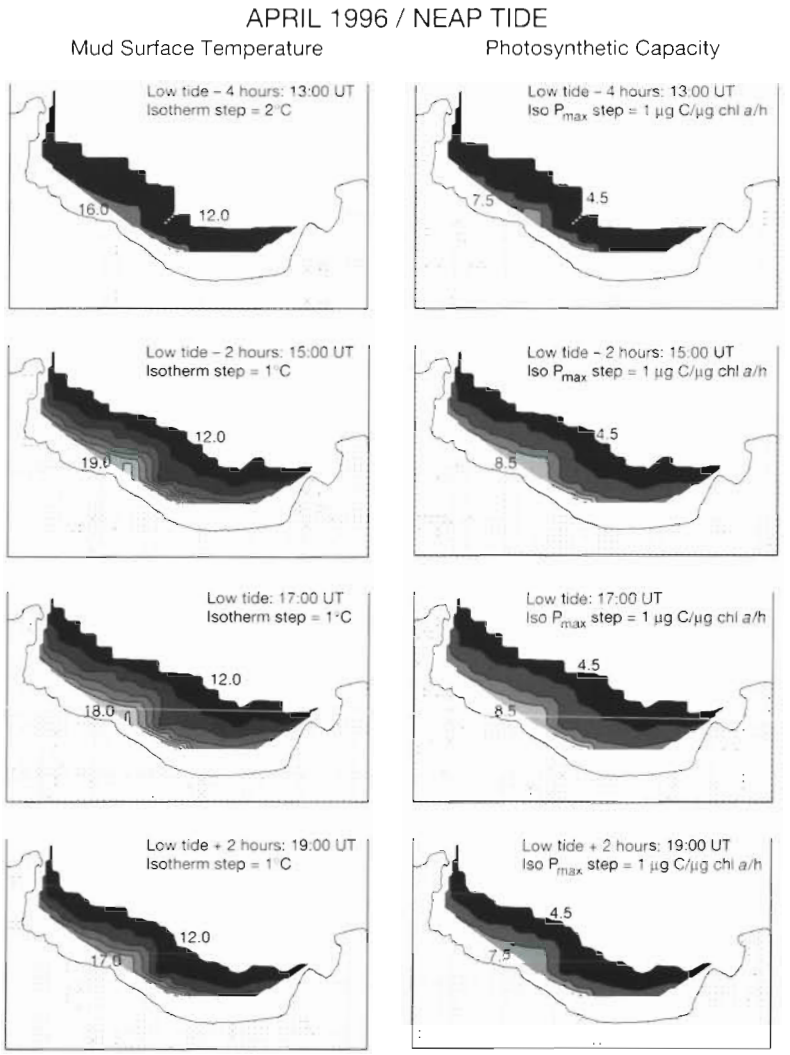

Fig. 5. Simulation of the spatio-temporal dynamics of MST and P^{B}_{max} in April 1996, neap tide

until low tide. The maximum value of P^{B}_{max} is the same as at spring tide [7.60 µg C (µg chl *a*)$^{-1}$ h^{-1}].

At the time of maximum inhibition, about 75% of the flat surface area is inhibited during spring tide whereas there is only about 20% at neap tide. P^{B}_{max} is also affected differently: it is only a few percent lower than its optimal value at neap tide [P^{B}_{MAX} = 7.60 µg C (µg chl *a*)$^{-1}$ h^{-1} at T_{opt} = 25.3°C; Table 2], whereas it is about 70% lower than the same optimal value at spring tide.

DISCUSSION

MST model

In the present paper, the MST model is based on a simplified thermodynamic approach accounting for the main processes controlling the heat exchange. Alternatively, MST could also be predicted by using empirical laws based on statistical relationships between meteorological data and soil surface characteristics (Gupta et al. 1981 and references cited therein). However, in spite of its simplicity, such an approach is inappropriate for spatial studies dealing with steep gradients because a new parameterization or even a new formulation is then required at each point.

The model predicts MST evolution with a good precision (Fig. 3, Table 3). However, 3 parameters closely related to mud properties (emissivity, ε_M; heat capacity, C_{P_M}; and porosity, ξ) are likely to fluctuate spatially. For instance, ε_M and C_{P_M} vary with the sediment organic content and the porosity (van Boxel 1986), while the porosity is itself controlled by the grain size and bioturbation. For practical reasons, the 3 parameters are held constant, but it is worth checking whether model predictions are affected by a small change of any of these parameters or not. This is done by performing a sensitivity analysis, and comparing the deviance D due to a perturbation of any of the 3 parameters P_i with the prediction error of the optimized model. The deviance D is defined as follows:

$$D = \frac{1}{N}\sum_{i=1}^{N}\sqrt{(MST_{i,dist} - MST_{i,nom})^2}$$

N = 1000

where MST_{dist} and MST_{nom} are temperature computed with perturbed and nominal values of P_i, respectively. Each P_i is selected within a range of values whose extremes are found in the literature for mud emissivity (van Bavel & Hillel 1976, Stathers et al. 1988), are given by *in situ* measurements for the porosity, and are given by the set of values estimated from the data series for the heat capacity (Table 3). Then, according to Miller (1974), the sensitivity of the model to the values of P_i is expressed by $S_i = \partial D/\partial P_i$ (assuming a local linearization at the nominal values P_{i0}). Relative sensitivity coefficients $R_i = S_i P_{i0}$ are given by percentages in Table 4. Results show that D is always lower than the prediction error (Table 3), and that the model is the least affected by the porosity (although it is the most variable parameter, see Table 4). Therefore, the model is poorly sensitive to the fluctuations of P_i in the range of admissible values considered.

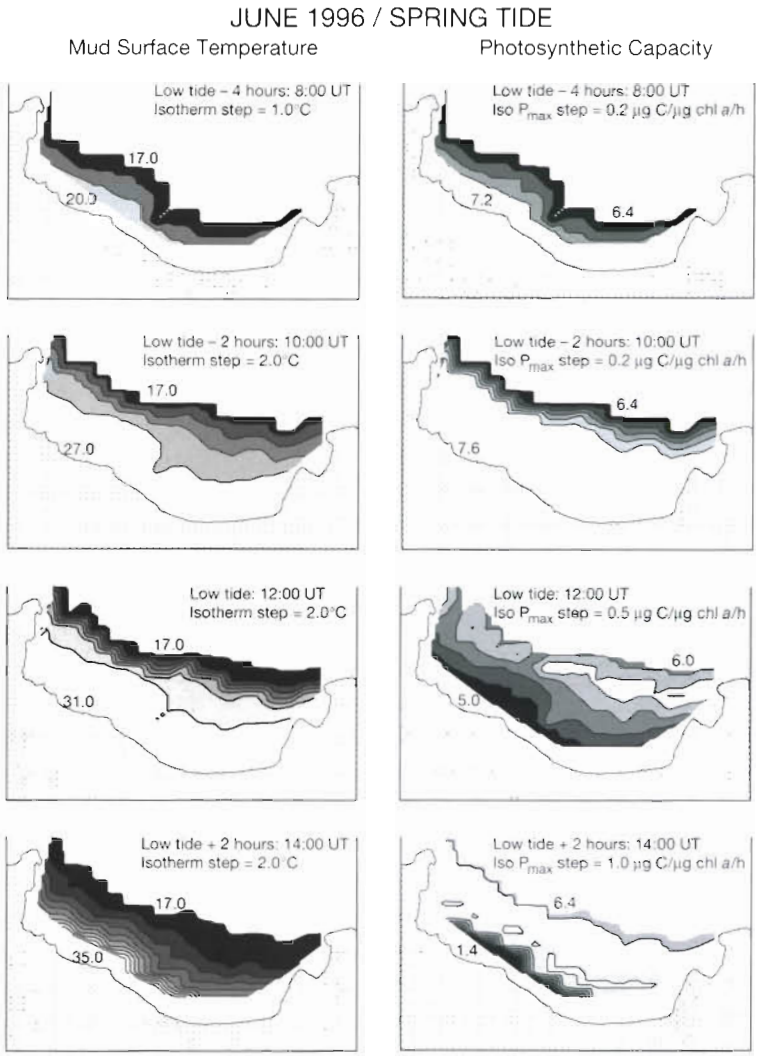

Fig. 6. Simulation of the spatio-temporal dynamics of MST and P^B_{max} in June 1996, spring tide

As during emersion MST is always in a non-steady state (as suggested by the influence of the phase difference between the tidal and sun cycles), the initial conditions must be accurately assessed (i.e. MST during immersion which rapidly reaches an equilibrium with the water temperature) (van Boxel 1986, Harrison & Phizacklea 1987). In this model, the water temperature is then forced by a data series measured at the boundary of the study area, but no horizontal gradient between MST and water temperature (due to the fast equilibrium between mud and water temperatures) is accounted for. This approximation is valid because the horizontal and vertical mixing is large enough to assume that this gradient is negligible at the spatial and temporal scales of the simulations (van Boxel 1986).

MST dynamics

The temporal dynamics of MST is characterized by 3 scales of variation (Fig. 3): long-term (seasonal), medium-term (within the 14 d lunar cycle) and short-term (within the day due to the succession of immersion-emersion periods). There are also interactions among scales so that short-term variations are determined by higher scales. For instance, the range of temperature change, the maxima and the rate of daily temperature increase are indeed dependent on both the time of the lunar cycle and the season. However, medium-term variations can be hidden by the prevalent influence of the meteorological conditions (see the comparison of the 3 time series in Fig. 3). Therefore, in order to assess the pattern of variability relevant to each scale, the within-day meteorological fluctuations have been filtered out. Accordingly, Fig. 8 shows the temporal dynamics of MST throughout 1 yr, at different levels of the mudflat; the influence of the topographic levels (equivalently, the emersion duration) is clearly pointed out. Overall, the spatio-temporal dynamics of MST is primarily controlled by the combination of the tidal and sun cycles, and particularly by the phase difference between them. the highest MSTs are achieved in summer in the highest parts of the mudflat at spring tide when low tide coincides with midday (Figs. 6 & 8).

P^B_{max} dynamics

The MST model allows computation of the instantaneous values of the temperature-dependent biomass-specific photosynthetic capacity of microphytobenthos

Table 4. Results of the sensitivity analysis. The relative sensitivity coefficient $R_i = (S_i P_{i0})$ is presented for each simulated time series. It represents the variation of D due to a 5% change in the value of $C_{P_{Ni}}$, ε_{Ni} or ξ. R_i allows to sort the relative influence of each parameter on the model sensitivity. The deviance D (°C) is calculated for a maximum disturbance of each parameter on the 3 time series, independently

Parameter	Mean	SD	R_i			D		
			March	May	June	March	May	June
$C_{P_{Ni}}$	612.0	20.19	2.88	1.96	2.42	0.57	0.32	0.52
ε_{Ni}	0.95	0.017	2.99	2.37	2.61	0.67	0.43	0.27
ξ	0.55	0.05	1.50	0.96	1.25	0.84	0.73	0.38

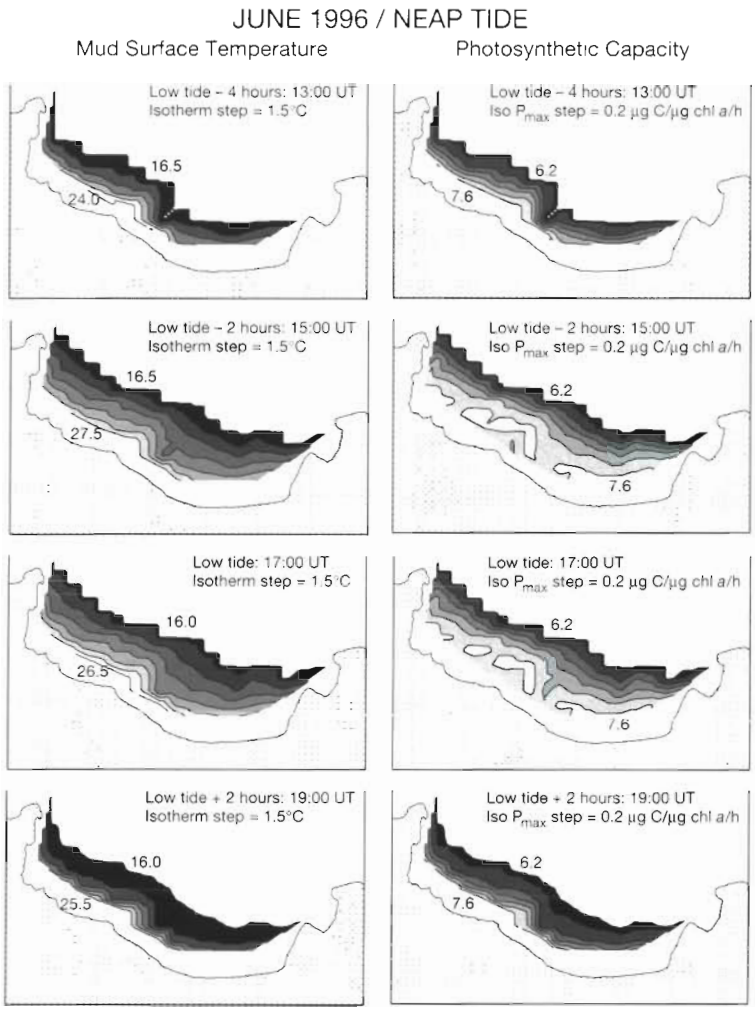

Fig. 7. Simulation of the spatio-temporal dynamics of MST and P^B_{max} in June 1996, neap tide

over the whole mudflat. The physiological parameters of P^B_{max} model (Table 2) were determined by laboratory experiments (Blanchard et al. 1996, in press).

It is clear from the results (Figs. 4 to 7) that the overall response of P^B_{max} to MST is strongly controlled by the optimum temperature value T_{opt}. In April, when the range of simulated MST remains below T_{opt} (25°C), P^B_{max} exhibits almost proportional changes with MST (Figs. 4 & 5). Conversely, in June, when the range of MST partially exceeds the optimum temperature (see Fig. 8), P^B_{max} is inhibited by the supra-optimal temperatures on most of the mudflat surface area (Figs. 6 & 7). This thermo-inhibition is all the more important in space and time when the phase difference between the tidal and sun cycles is small.

This is a very important issue since in such conditions the level of the photosynthetic capacity is lower than in April. The inhibition is due to the fact that microphytobenthos exhibits the same T_{opt} throughout the year although the temperature environment changes. This absence of acclimation is in contrast to what usually occurs in phytoplankton (Li 1980), and the likely reasons of this paradox are discussed elsewhere (Blanchard et al. in press): it is hypothesized therein that T_{opt} is prevented from fully adjusting to ambient temperatures because microalgae are in a very fluctuating thermal environment; the temperature range of variations at high frequency (hourly changes during emersion) is of the same order of magnitude as the temperature change at low frequency (between winter and summer). In addition, due to resuspension-transport-deposition during high tide, microalgae can move over large distances (from low levels to high levels and vice versa) on the mudflat. They can thus experience very different MST changes from one low tide to the next depending on their successive positions on the mudflat. By the way, this emphasizes that the dynamics of microphytobenthos is also related to the sedimentary dynamics.

As the ecological consequences of thermo-inhibition may be important, it is necessary to determine the frequency of these events during the year According to the T_{opt} value, it is clear from Fig. 8 that inhibition is likely to occur from May to September in the highest levels of the mudflat. The frequency diagram of hourly values of MST—during the diurnal emersion periods only—shows that ca 10% of them correspond to thermo-inhibitory conditions at the highest level. In summer, thermo-inhibition becomes a prominent feature of microphytobenthos photosynthesis. Even though we cannot establish a causal link, this result has nevertheless to be compared with the summer depression of microphytobenthos biomass which has been observed both in the Dollard estuary (Cadée & Hegeman 1974, Colijn & Dijkema 1981) and in the Bay of Marennes-Oléron (Cariou-Le Gall & Blanchard 1995). This depression is generally ascribed to the grazing of invertebrates which could overcome the production rates during summer, and to a lesser extent to nutrient depletion. Therefore, thermo-inhibition is not directly responsible for the biomass depression but induces a decrease of production which cannot then balance mortality. In contrast, Admiraal & Peletier (1980) conclude that temperature in the Dollard estuary is not responsible for the summer depression in biomass because they measured the highest growth rates of cultures incubated on the mud-

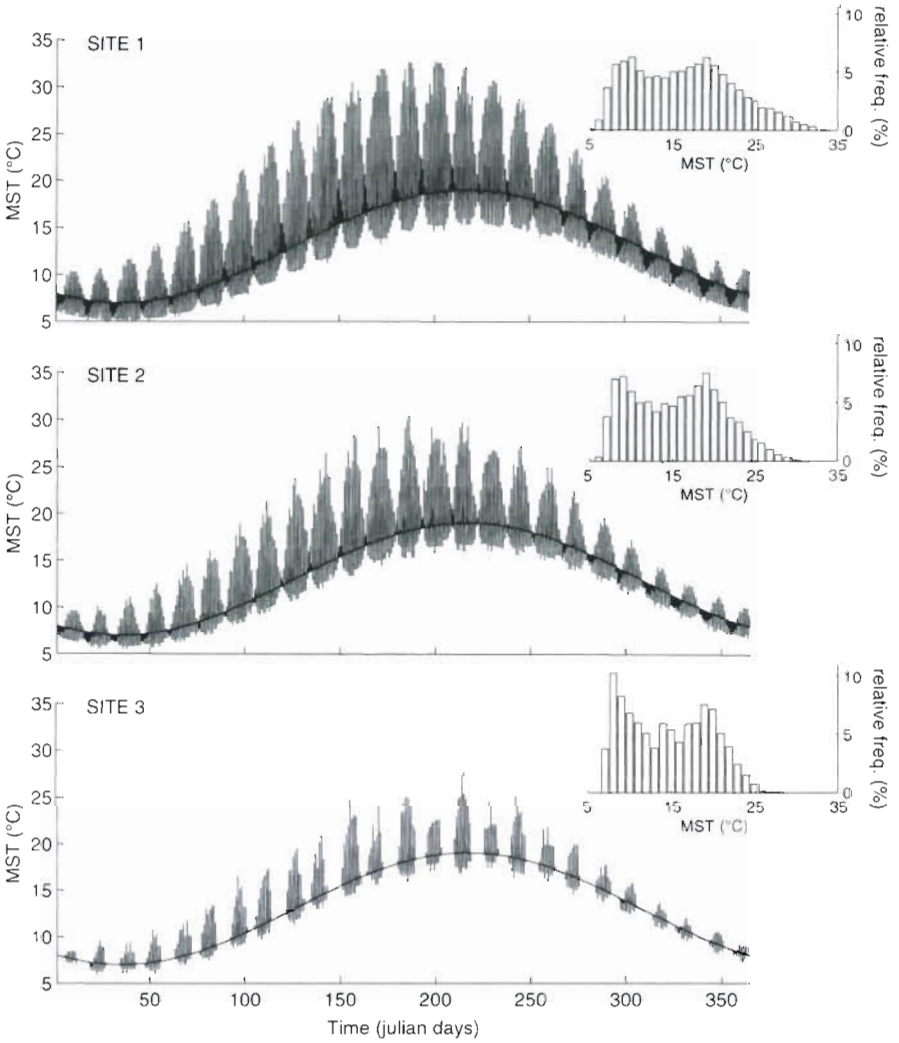

Fig. 8. Simulation of MST variations during the whole of 1996. For each month, an 'average meteorological day' is used (see text). Simulations are performed for different levels on the mudflat (see location on the map of Fig. 1). The relative frequency histograms of hourly values of MST (inset) refer to the diurnal emersion periods only

flat in June when the air temperature reached 29°C. It is worth noting, however, that growth rates (based on the cell division rate) and photosynthetic capacities (based on the instantaneous carbon assimilation) do not refer to the same time scales and, as such, are not directly comparable. The debate is thus still open on whether thermo-inhibition of the photosynthetic capacity can affect significantly the growth rate of benthic microalgae and lead to a biomass depression in the summer period. The ecological stakes are important and deserve more investigations from ecologists in the near future.

Acknowledgements. We are very grateful to Dr P. Richard for providing us with a map of the study site and to Dr C. Bacher for his valuable comments. We are indebted to Dr P. Le Hir for permitting us to use his hydrodynamic model, and to C. Chevalier for providing us with the meteorological data series. The study was financially supported by the Centre National de la Recherche Scientifique (CNRS), the Institut Français de Recherche et d'Exploitation de la Mer (IFREMER), the Région Poitou-Charentes, and the European Community (contract No. MAS3-CT95-0022, INTRMUD).

LITERATURE CITED

Admiraal W, Peletier H (1980) Influence of seasonal variations of temperature and light on the growth rate of cultures and natural populations of intertidal diatoms. Mar Ecol Prog Ser 2:35–43

Baillie PW, Welsh BL (1980) The effect of tidal resuspension on the distribution of intertidal epipelic algae in an estuary. Estuar Coast Shelf Sci 10:165–180

Blanchard GF, Cariou-Le Gall V (1994) Photosynthetic characteristics of microphytobenthos in Marennes-Oléron Bay, France: preliminary results. J Exp Mar Biol Ecol 182: 1–14

Blanchard GF, Guarini JM (1996) Studying the role of mud temperature on the hourly variation of the photosynthetic capacity of microphytobenthos in intertidal areas. C R Acad Sci Paris Life Sci 319:1153–1158

Blanchard GF, Guarini JM, Gros Ph, Richard P (in press) Seasonal effect on the relationship between the photosynthetic capacity of intertidal microphytobenthos and temperature. J Phycol

Blanchard GF, Guarini JM, Richard P, Gros Ph, Mornet F (1996) Quantifying the short-term temperature effect on light-saturated photosynthesis of intertidal microphytobenthos. Mar Ecol Prog Ser 134:309–313

Brock TD (1981) Calculating solar radiation for ecological sudies. Ecol Model 14:1–19

Businger JA (1973) Turbulent transfer in the atmospheric surface layer. In: Haugen DA (ed) Workshop on micrometeorology. Am Met Soc, Boston, MA, p 67–100

Cadée GC, Hegeman J (1974) Primary production of the benthic microflora living on tidal flats in the Dutch Wadden Sea. Neth J Sea Res 8:2–3

Cariou-Le Gall V, Blanchard GF (1995) Monthly HPLC measurements of pigment concentration from an intertidal muddy sediment of Marennes-Oléron Bay, France. Mar Ecol Prog Ser 121:171–179

Colijn F, de Jonge VN (1984) Primary production of microphytobenthos in the Ems-Dollard Estuary. Mar Ecol Prog Ser 14:185–196

Colijn F, Dijkema KS (1981) Species composition of benthic diatoms and distribution of chlorophyll *a* on an intertidal flat in the Dutch Wadden Sea. Mar Ecol Prog Ser 4:9–21

de Jonge VN, Colijn F (1994) Dynamics of microphytobenthos biomass in the Ems estuary. Mar Ecol Prog Ser 104: 185–196

de Jonge VN, van Beusekom JEE (1992) Contribution of resuspended microphytobenthos to total phytoplankton in the Ems estuary and its possible role for grazers. Neth J Sea Res 30:91–105

Gupta SC, Radke JK, Larson WE (1981) Predicting temperatures of bare and residue covered soils with and without a corn crop. Soil Sci Soc Am J 45:405–412

Harrison SJ (1985) Heat exchanges in muddy intertidal sediments: Chichester Harbour, West Sussex, England. Estuar Coast Shelf Sci 20:477–490

Harrison SJ, Phizacklea AP (1987) Vertical temperature gradients in muddy intertidal sediments in the Forth estuary, Scotland. Limnol Oceanogr 32:954–963

Le Hir P, Bassoullet P, L'Yavanc J (1993) Application of a multivariate transport model for understanding cohesive sediment dynamics. In: Mehta AJ (ed) Nearshore and estuarine cohesive sediment transport. Coastal and estuarine studies, American Geophysical Union, Washington, DC, 42:467–485

Levinton JS, Bianchi TS (1981) Nutrition and food limitation of deposit feeders, 1. The role of microbes in the growth of mud snails. J Mar Res 39:531–545

This article was submitted to the editor

Li WKW (1980) Temperature adaptation in phytoplankton: cellular and photosynthetic characteristics. In: Falkowski PG (ed) Primary production in the sea. Plenum Press, New York, p 259–279

Losordo TM, Piedrahita RH (1991) Modelling temperature variation and thermal stratification in shallow aquaculture ponds. Ecol Model 54:189–226

Miller DR (1974) Sensitivity analysis and validation of simulation models. J Theor Biol 48:345–360

Nelder VA, Mead R (1965) A simplex method for function minimization. Computer J 7:308–313

Paterson DM (1989) Short-term changes in the erodibility of intertidal cohesive sediments related to the migratory behavior of epipelic diatoms. Limnol Oceanogr 34: 223–234

Piccolo MC, Perillo GME, Daborn GR (1993) Soil temperature variations on a tidal flat in Minas Basin, Bay of Fundy, Canada. Estuar Coast Shelf Sci 35:345–357

Pikul JL Jr (1991) Estimating soil surface temperature from meteorological data. Soil Sci 151:187–195

Pinckney J, Zingmark RG (1991) Effects of tidal stage and sun angles on intertidal benthic microalgal productivity. Mar Ecol Prog Ser 76:81–89

Plante-Cuny MR, Plante R (1986) Benthic marine diatoms as food for benthic marine animals. In: Ricard M (ed) Proc 8th Int Diatom Symposium, Paris, 1984. Koeltz, Koenigstein, p 525–537

Pond S, Fissel DB, Paulson CA (1974) A note on bulkaerodynamic coefficients for sensible heat and moisture flux. Boundary-Layer Meteorol 6:333–339

Priestley CHB (1959) Heat conduction and temperature profiles in air and soil. J Aust Inst Agric Sci 25:94–107

Stathers RJ, Black TA, Bailey WG, Novak MD (1988) Modelling surface energy fluxes and temperatures in dry and wet bare soils. Atmosphere-Ocean 26:59–73

van Bavel CHM, Hillel DI (1976) Calculating potential and actual evaporation from a bare soil surface by simulation of concurrent flow of water and heat. Agric Meteor 17: 453–476

van Boxel JH (1986) Heat balance investigations in tidal areas. PhD thesis, Univ Amsterdam

Vugts HF, Zimmerman JTF (1985) Heat balance of a tidal flat area. Neth J Sea Res 19:1–14

Manuscript first received: March 7, 1997
Revised version accepted: May 5, 1997